Journal of Materials Science & Technology 34 (2018) 1405–1411

Contents lists available at ScienceDirect

Journal of Materials Science & Technology

journal homepage: www.jmst.org

Achieving the high phase purity of $CH_3NH_3PbI_3$ film by two-step solution processable crystal engineering

Yan Li, Bin Ding, Guan-Jun Yang*, Chang-Jiu Li, Cheng-Xin Li

State Key Laboratory for Mechanical Behavior of Materials, School of Materials Science and Engineering, Xi'an Jiaotong University, Xi'an 710049, China

ARTICLE INFO

Article history:
Received 16 May 2017
Received in revised form 27 May 2017
Accepted 27 May 2017
Available online 2 November 2017

Keywords:
High phase purity
$CH_3NH_3PbI_3$ film
Two-step solution method
Perovskite solar cells

ABSTRACT

To date, it is still a great challenge for highly efficient perovskite devices to realize the high quality perovskite films with high purity, high coverage ratio and good crystallization by two-step scalable solution method. In this study, a series PbI_2 films with tunable micro-architecture of PbI_2 crystals are prepared via solution processable crystal engineering. The perovskite film, prepared by optimized pit spacing in gas pumped PbI_2 film at 1000 Pa, shows the highest film quality, including no residual PbI_2 phase, compact morphology, and improved photoluminescence intensity. A transformation kinetics shows that the pit spacing strongly influences both the mass transfer and the sequential intercalation reaction between CH_3NH_3I and PbI_2 crystals, which ultimately determines the full reaction state of the perovskite film. The perovskite solar cells assembled by the perovskite film show both high power-conversion efficiency and good reproducibility of photovoltaic performance due to the restrained charge recombination arising from the high quality perovskite film.

1. Introduction

The perovskite solar cells (PSCs) are presently under intense investigation for their low cost, easy fabrication and high efficiency. In 2009, the perovskite material was introduced as a sensitizer in dye-sensitized solar cells (DSCs) for the first time, however, it only showed a transient conversion efficiency of 3.8% due to the dissolution of the perovskite in liquid electrolyte [1]. Until 2012, the all solid state PSCs were successfully proposed by Park et al. [2], which provided a new idea for the further development of PSCs. Nowadays, the PSCs as an exciting alternative to the traditional DSCs routinely show power-conversion efficiencies exceeding 20%, and this progress makes the PSCs attracted considerable attention [3–7]. The excellent photovoltaic performance of PSCs, especially the planar heterojunction solar cell, depends on the high quality of perovskite film, such as high phase purity, full coverage state and good crystallization. Otherwise, both deleterious impacts and shunting pathways to charge dissociation, transport, as well as recombination will be introduced and result in the degradation of device performance [8,9].

Two-step solution method is one of the low-cost and easy fabrication methods to produce a perovskite film [10,11]. Generally, the two-step solution method for fabricating $CH_3NH_3PbI_3$ films can be mainly divided into two stages: (a) Preparing the PbI_2 film, (b) Dipping the PbI_2 film into a CH_3NH_3I solution to form a perovskite film. Usually, the dipping time of stage (b) is short, or the prolonged dipping time will induce the dissolution and recrystallization of the as-prepared perovskite film, which even leads to peel-off of the perovskite film into the solution [12–14]. Based on the limited dipping time, there is always residual unreacted PbI_2 in the final perovskite film. The residual PbI_2 in the final perovskite film, significantly harm not only the long term stability of the perovskite film [15,16], but also the cell performance and its reproducibility [17–19].

To realize the high phase purity of the perovskite film, many efforts have been tried to modify the dipping stage, such as, vapor-assisted solution process and solvent annealing [20,21]. However, these projects need not only a long reaction time but also a precise precursor stoichiometry. In addition, Wu et al. [18] changed the PbI_2 film into uncrystallized state using the dimethylsulfoxide as solvent, and the strategy efficiently enhanced the sufficient reaction of PbI_2 films during two-step solution method. The result illustrates that the packing state of the PbI_2 crystals in the PbI_2 film has a strong influence to its transformation process during two-step solution method. Furthermore, previous results have shown that manipulating the packing state of the PbI_2 crystals, indicating increasing the porosity of PbI_2 film, could effectively enhance the transformation process compared with the traditional compact PbI_2 film during two-step solution method [19,22–24]. For example, El-Henafwey et al. [19] introduced pores into the PbI_2 film by modifying the preparation process with toluene and chlorobenzene

* Corresponding author.
E-mail address: ygj@mail.xjtu.edu.cn (G.-J. Yang).

https://doi.org/10.1016/j.jmst.2017.11.003
1005-0302/

vapors treatment, and Cao et al. [22] introduced pores into the PbI_2 film by releasing the thermally unstable methylammonium acetate in the precursor film, both of which enabled large surface areas of PbI_2 films for reaction with CH_3NH_3I and accelerated perovskite film reaction process.

Based on all the above, increasing the porosity of the traditional compact PbI_2 film could significantly enhance the transformation kinetics during dipping state. However, until now, it is still a great challenge to directly tuning the microstructures of the PbI_2 films, including grain size of PbI_2 crystals and the corresponding porosity of PbI_2 film, during pure solution engineering, and the fundamental physics of the transformation kinetics between the microstructure of PbI_2 films and its sufficient reaction state are still unclear.

In this study, the PbI_2 films with tunable micro-architecture, *i.e.*, pit spacing, were prepared by a gas pumping process under various drying pressures, and the transformation kinetics of PbI_2 films were detailed discussed. The results showed that there was an intimate relationship between the microstructure of PbI_2 films and their transformation states. At last, the PSCs assembled with the PbI_2 films under the drying pressure of 1000 Pa showed both higher power-conversion efficiency and a much better reproducibility of photovoltaic performance due to the restrained charge recombination arising from the high phase purity, high coverage ratio and good crystallization of the perovskite films.

2. Experimental

2.1. Solution and film preparation

Lead iodide (PbI_2) and methylammonium (CH_3NH_3I) purchased from Weihua Solar Energy Co. (China) were used as solute. 2-propanol and N, N-dimethylformamide (DMF) were purchased from Acros (Germany) and Sigma-Aldrich (Germany) separately, which were used as solvent. All the chemicals were reagent grade and used without further purification. The transparent fluorine-doped tin oxide (FTO, TEC-15, LOF) conductive glasses (25 mm × 25 mm) were employed as substrates. Before the film deposition, the substrates were cleaned in successive ultrasonic acetone and alcohol bath followed by drying using high purity N_2 flow.

For precursor solution preparation, PbI_2 was dissolved in DMF solvent with a concentration of 460 $mg{\cdot}ml^{-1}$, and then kept at 70 °C for more than 8 h by using laboratory type magnetic stirrer. CH_3NH_3I was dissolved in 2-propanol solvents with a concentration of 20 $mg{\cdot}ml^{-1}$, and then stirred for more than 8 h by a laboratory type magnetic stirrer. Before perovskite film preparation, both precursor solutions were filtered using PTEE filter with a pore size of 0.2 μm. The perovskite film was prepared by the following steps. Firstly, the PbI_2 precursor solution was dropped on the substrate surface and spin-coated at 4000 rpm for 10 s, and then it was dried under natural drying condition or at different gas pumping pressures (3000, 1000, and 40 Pa) [25]. The chamber pressures are controlled automatically by the equipment control unit. Secondly, the films were dipped in the CH_3NH_3I precursor solution for 60 s. Thirdly, the films were rinsed with pure 2-propanol, and dried by compressed N_2 flow. All the processes were carried out in the air without inert gas protection. During the film preparation the laboratory temperature was kept below 25 °C.

2.2. Device fabrication

A compact layer of ZnO was deposited on the etched FTO substrate (ZnO/FTO substrate) by ion sputtering and then annealed at 120 °C for 15 min. Subsequently, the substrates were treated in UV/O_3 cleaner machine for 15 min. The perovskite film was deposited on the compact ZnO/FTO substrate by two-step solution method as illustrated in the former section. After the as-prepared film was annealed at 100 °C for 10 min, the 2, 2′, 7, 7′ – tetrakis(N,N-di-*p*-methoxyphenylamine) – 9, 9′ – spirobifluorene (Spiro-OMeTAD) based hole transport layer (HTM) was deposited by spin coating at 3000 rpm for 30 s, where the HTM solution consisted of 400 mg Spiro-OMeTAD, 142.5 μL 4-*tert*-butylpyridine and 87.5 μL lithium – bis(trifluoromethanesulfonyl)imide (Li-TFSI) in 5 mL chlorobenzene. The spiro-OMeTAD coated substrates were stored in an auto-drying cabinet at 20 °C with a relative humidity of 15% for 8 h. Finally, a 200 nm thick Au layer was deposited on the HTM layer by thermal evaporation.

2.3. Characterization

The surface morphologies of both PbI_2 films and perovskite films, and the sectional view of both PbI_2 films and perovskite films were examined by field emission scanning electron microscopy (FESEM, TESCAN, Czech Republic). The phase compositions of the perovskite films were measured by using an x-ray diffractometer (SHIMADZU, Japan) with Cu *K*α radiation. To quantitatively analyze the absorption ability of the perovskite films, an UV–vis spectrophotometer (Hitachi U-4100, Japan) was employed. The photoluminescence (PL) was measured by a steady state spectrophotometer (Fluoromax-4, Horiba Jobin Yvon, France) with excitation wavelength of 560 nm.

The photocurrent density-voltage (*J-V*) curves of the solar cells were measured by using a solar simulator (100 $mW{\cdot}cm^{-2}$, Oriel 94023A, Newport) equipped with a Keithley 2400 digital source meter. The exact light intensity was calibrated using a single-crystal silicon photovoltaic cell as the reference (91150 V, Oriel Instruments). The cells were measured with a metal mask covered with an area of 0.10 cm^2 to receive sunlight, and the scan step is 48.9 mV; the delay time is 1000 ms. The external quantum efficiency (EQE, Qtest Station 500AD, Crowntech, Inc.) spectra were tested using a solar cell spectral response/QE/IPCE test system in AC mode. To investigate the charge transport and recombination mechanism of the PSCs, the electrochemical impedance spectroscopy (EIS, Zennium IM6, Zahaner) was measured under illumination, with the frequency ranging from 4 MHz to 5 Hz and AC amplitude of 20 mV, with different bias voltages.

3. Results and discussion

3.1. Microstructures of PbI_2 films and perovskite films

The PbI_2 film was prepared by a conventional spin-coating and solvent evaporation method. After spin-coating, a gas pumping process was introduced to replace the natural drying condition to manipulate the microstructures of the film. In this study, the additional drying pressures of 3000, 1000 and 40 Pa were chosen to stand for the typical high, middle and low pressures. The as-prepared PbI_2 films were named as PbI_2-N.D., PbI_2-H.P., PbI_2-M.P. and PbI_2-L.P., and the corresponding perovskite films after dipping stage were named as PVK-N.D., PVK-H.P., PVK-M.P. and PVK-L.P.

. 1 shows the microstructures of PbI_2 films under various drying pressures and the corresponding perovskite films without annealing. As can be seen, under natural drying condition, the PbI_2 film shows a non-uniform morphology. The PbI_2 crystals tend to aggregate into a dendritic structure, leaving large scale of uncovered areas on the substrate. The low magnification of PbI_2-N.D. is shown in Fig. S1. When decreasing the drying pressure to 3000 Pa, the PbI_2 film shows a loosely packing state with obvious large grain size. When further decreasing the drying pressure to 1000 Pa, the grain size of PbI_2 crystals decrease. The higher magnification of the surface morphology for PbI_2-M.P. is shown in Fig. 2(a). At last, when

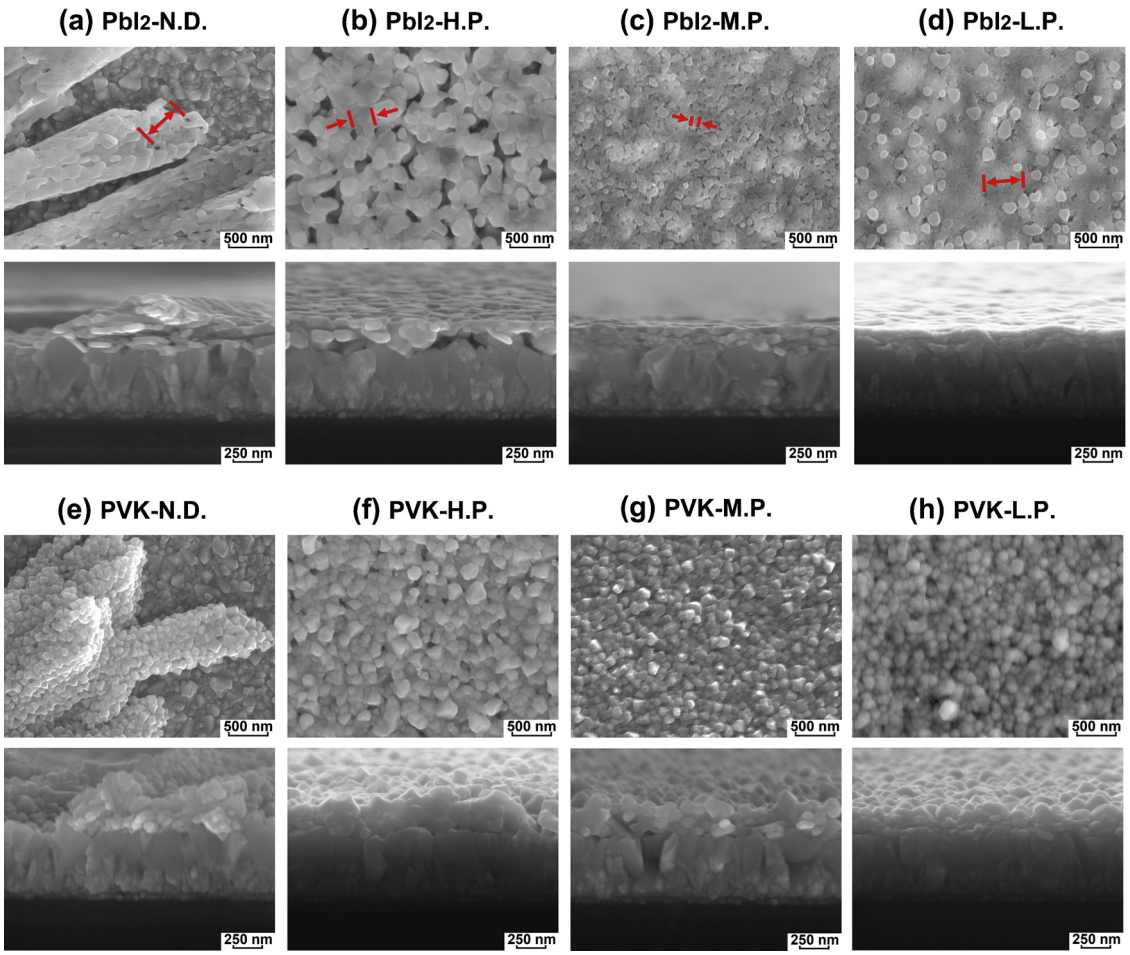

Fig. 1. Surface morphologies and the cross sectional view of PbI_2 films and the corresponding perovskite films: (a) PbI_2-N.D., (b) PbI_2-H.P., (c) PbI_2-M.P., (d) PbI_2-L.P., (e) PVK-N.D., (f) PVK- H.P., (g) PVK- M.P. and (h) PVK- L.P., where N.D. refers to natural drying; H.P. refers to high pressure drying; M.P. refers to middle pressure drying; L.P. refers to low pressure drying. The typical pit spacing of each PbI_2 film is marked with red signs. (For interpretation of the references to colour in this figure legend, the reader is referred to the web version of this article.)

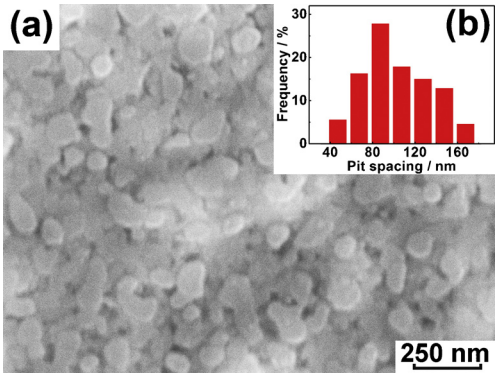

Fig. 2. High magnification of PbI_2-M.P. film (a) and the corresponding pit spacing (PS) distribution (b).

the drying pressure is decreased to 40 Pa, except that it seems some PbI_2 particles or PbI_2 slices on the surface of the film, the PbI_2 film shows a uniform, flat and tight pressed morphology.

Except the commonly grain size of PbI_2 film, based on the surface morphologies of the PbI_2 films, the distance between pits, indicating pit spacing (PS) is also changed. The typical PS of each PbI_2 film is shown as red signs in Fig. 1, and the statistical distribution of the PS for PbI_2-M.P. film is shown as Fig. 2(b) individually. As can be seen, the PS decreases with decreasing the drying pressure to 1000 Pa. However, when going on decreasing the drying pressure to 40 Pa, the PS increases, which is even larger than the PS of PbI_2-H.P.

Generally, the crystallization process is composed of super saturation, nucleation and growth up. Under natural drying condition, the crystal nuclei precipitation is limited, and the long solvent evaporation time will result in a long crystal growth time. There will be an overgrowth of original nuclei, which ultimately results in the solute accumulation in local areas [26], therefore, it shows a dendritic structure as shown in Fig. 1(a). Furthermore, it is known that decreasing the drying pressures of precursor solution leads to the rapid evaporation of the solvent, which will improve the degree of super saturation for the solution. The higher the degree of super saturation for the solution, the easier the crystal nuclei precipitation [27–30], which will yield an increased amount of nuclei in a short time. Therefore, based on the same weight of the solute after spin-coating, the increased amount of PbI_2 nuclei will induce the increased numbers of the PbI_2 crystals, and thereby yields a decreased grain sizes as shown in Fig. 1(b) to (c). When the drying pressure is low enough, the growth up is also enhanced by the high degree of super saturation, which may be playing a more important role to decrease the degree of super saturation compared with nucleation. Therefore, under drying pressure of 40 Pa, the PbI_2 film shows a contiguous morphology (Fig. 1(d)). It should be noted, based on the sectional view, the PbI_2-L.P. film shows a contiguous morphology without any PbI_2 particles or PbI_2 slices on the surface,

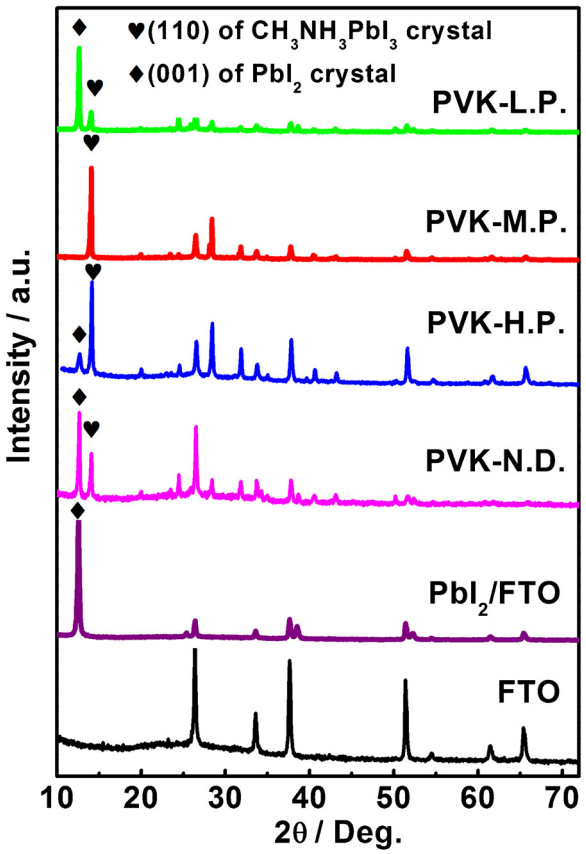

Fig. 3. XRD patterns of the FTO substrate, the PbI_2-N.D. film and the various perovskite films. These data were collected using PbI_2 and perovskite films formed on FTO substrates.

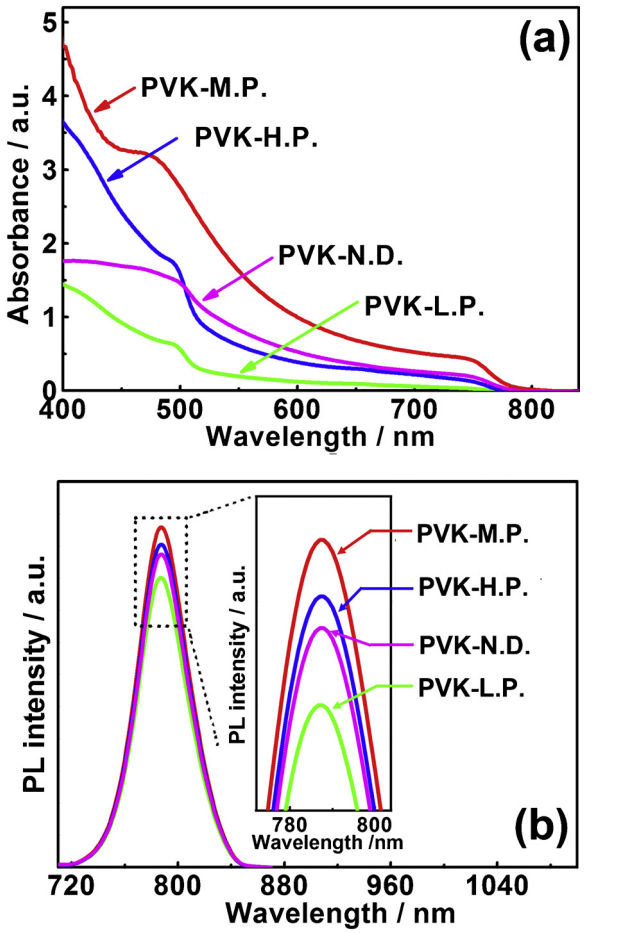

Fig. 4. UV–vis absorption spectrums (a) and the steady-state PL spectra (b) of the perovskite films with the architecture of perovskite film/glass.

which illustrate that the PbI_2 particles or PbI_2 slices with limited height are not independent of the surface for PbI_2-L.P. film.

After the dipping stage, as shown in Fig. 1(e)–(h), the perovskite films show a more and more compact morphology. When the drying pressure decreases to 3000 Pa, the perovskite film shows some voids in the surface morphology of the perovskite film, which may result in the shunt path in the assembled solar cells. When the drying pressure goes on decreasing to 1000 Pa, there is hardly any non-connected area in the perovskite film. In addition, when the drying pressure of PbI_2 film is above 1000 Pa, the perovskite crystals show a specific cubic morphology [31–33]. However, when the drying pressure decreases to 40 Pa, the perovskite crystals press against each other showing sphere crown morphology, and such a particular appearance seems to be the unshaped cubic perovskite crystals.

Compared with the cross sectional views of the PbI_2 films and the corresponding perovskite films, when the drying pressures are above 1000 Pa, the morphology of PbI_2 crystals across cross section of the PbI_2 film is obviously changed after the dipping stage. However, when the drying pressure decreased to 40 Pa, only the PbI_2 crystals on the surface of the PbI_2 films show the change in morphology, whereas the PbI_2 crystals in the deep area of the PbI_2 film are almost the same.

3.2. *Phase structure and absorption of perovskite films*

X-ray diffraction was performed to investigate the phase purity of the PbI_2 films and the corresponding perovskite films, as shown in Fig. 3 and Fig. S2. The crystallization of pure PbI_2 films drying under various conditions show the consistent diffraction patterns. All of them show a strong diffraction peak at the 2θ of 12.7°, corresponding to (001) crystal plane of PbI_2 crystals [34]. After dipping stage, compared with the pure PbI_2 film, there is an apparent diffraction peak at the 2θ of 14.2° appearing in the XRD patterns. The diffraction peak is assigned to the (110) crystal plane of $CH_3NH_3PbI_3$, which indicates the transformation of PbI_2 into $CH_3NH_3PbI_3$ [35]. Comprehensively compared the diffraction intensity of PbI_2 and $CH_3NH_3PbI_3$ in the perovskite films, it can be seen that the content of $CH_3NH_3PbI_3$ increases, whereas the content of the residual PbI_2 decreases to disappear (PVK-M.P.) with decreasing of the drying pressures of PbI_2 films. However, when going on decreasing the drying pressure of PbI_2 film to 40 Pa, only a little fraction of $CH_3NH_3PbI_3$ appears, leaving a large portion of unreacted PbI_2 in the perovskite film.

Considering the absorbance ability of the perovskite films will be strongly influenced by the content of $CH_3NH_3PbI_3$ [36], to further evaluate the phase purity of the perovskite films, the UV–vis absorption spectra were measured as shown in Fig. 4(a). As it can be seen in Fig. 4(a), the optical property is consistent with the XRD results. When the drying pressure of PbI_2 films is above 1000 Pa, the absorption intensity of perovskite films is increased with decreasing of drying pressures. However, when going on decreasing the drying pressure of PbI_2 film to 40 Pa, the absorption intensity of perovskite films decreases.

The PL measurements were also performed to characterize the crystallization of the perovskite films as shown in Fig. 4(b). The PVK-M.P. shows the strongest PL intensity compared with the other perovskite films, which illustrate that the PVK-M.P. has an improved crystallization which may be attributed to the low defects

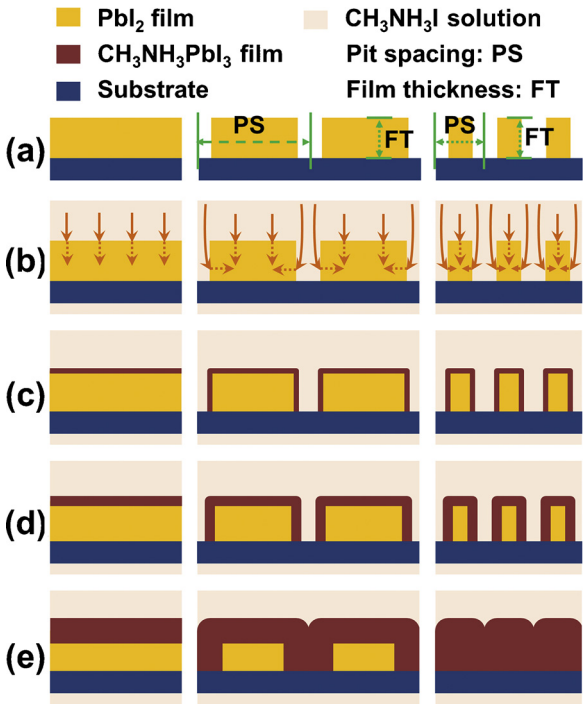

Fig. 5. Schematic illustration of the transformation kinetics of PbI_2 films with various microstructures: (a) PbI_2 films with various microstructures: compact PbI_2 film, 1/2 PS > FT and 1/2 PS < FT (from left to right), (b) the diffusion path of CH_3NH_3I, (c), (d) and (e) the reaction processes with prolonging the dipping time.

resulting from the sufficient reaction state and the compact morphology.

3.3. *Transformation kinetics of PbI_2 films with various micro-architectures*

The as-prepared PbI_2 crystal is sandwiched by multilayer of I-Pb-I into 2H structure [37], which is an open architecture for the intercalation process. During the dipping stage, the intercalation reaction proceeds from the surface to the center of the PbI_2 crystals to form into $CH_3NH_3PbI_3$ [38]. When the PbI_2 crystals stack together, the porous PbI_2 film is formed. The porous PbI_2 film is equivalent to the compact PbI_2 film which is dug into pores in the inset of the film. Though manipulate the distribution of the pores, indicating the distances of the pores, the PbI_2 films with various microstructures are realized.

To systematically evaluate the variations of the porous PbI_2 films, the surface morphology of the PbI_2 films are considered. Though the connected pores in the inside of the PbI_2 film will outcrop in the surface morphology, definitely, only the pits and the corresponding pit spacing (distance between pits, PS) will be got from the two – dimensional surface morphologies of the PbI_2 film. Therefore, objectively, the PS is proposed to illustrate the evolution of the microstructures for PbI_2 films.

To investigate the influence of PS to the transformation kinetics of PbI_2 film into $CH_3NH_3PbI_3$ film, the porous PbI_2 films can be divided into three situations, which are shown in Fig. 5(a). When the PS is infinitely great, the PbI_2 film will have a compact morphology. With decreasing the PS, the 1/2 PS will be gradually changed from larger than film thickness (FT) to smaller than FT, and the corresponding PbI_2 films are named as 1/2 PS < FT and 1/2 PS > FT. With adding pores in the PbI_2 film, the surface of the porous PbI_2 film will divided into outside surface and inner surface compared with the compact PbI_2 film. When the PbI_2 films are dipped into CH_3NH_3I solution (Fig. 5(b)), the full reaction state of the PbI_2 films depend

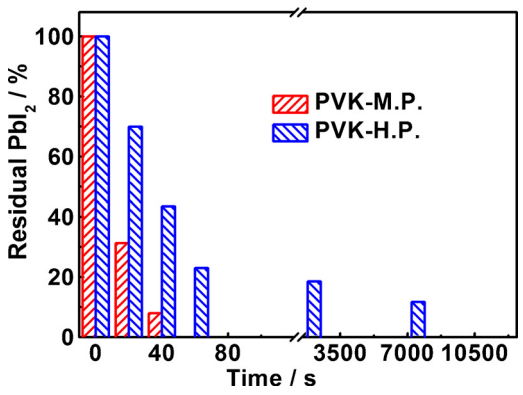

Fig. 6. Calculated results of the residual PbI_2 in PVK-M.P. film and PVK-H.P. film according to the XRD patterns under different dipping time.

on the mass transfer of the CH_3NH_3I. The mass transfer of CH_3NH_3I chemical can be divided into two steps: Firstly, the CH_3NH_3I diffuses to both the outside surface and inner surface; Secondly, the CH_3NH_3I diffuses into the deep direction of PbI_2 to realize the phase transformation.

The detailed reaction processes of PbI_2 films with different PSs by prolonging the dipping time are also discussed as shown in Fig. 5(c)–(e). At the beginning, the surface, including outside surface and inner surface, of PbI_2 film is transformed into $CH_3NH_3PbI_3$ (Fig. 5(c)). With increasing of the dipping time, the intercalation reaction goes on to the deep direction (Fig. 5(d)). At last, for PbI_2 film of 1/2 PS < FT, through the inner surface enhance the degree of the intercalation reaction for the increased surface area compared with compact PbI_2 film, the final full reaction state of them are both depended on the diffusion of CH_3NH_3I in the film thickness direction. For the film of 1/2 PS > FT, the limited PS of the PbI_2 film not only increases surface areas, but also decreases the effective diffusion length of CH_3NH_3I in the PbI_2 film, which ultimately realize the full reaction state.

Based on the typical PS marked with red signs for each PbI_2 film at Fig. 1, under natural drying condition and drying pressure of 3000 Pa, the large PS for the PbI_2-N.D. and PbI_2-H.P. results in the long intercalation reaction routing, which will result in the non-full reaction state for both films during dipping time of 60 s. Much effort was also made to extend the dipping time to 30 min for the PbI_2-H.P. film, but the PbI_2 phase could not be easily removed from the perovskite film. At last, when we prolonged the dipping time to 3 h for PbI_2-H.P. film, there was no PbI_2 peak in the XRD patterns. However, the final PVK-H.P. film showed a serious dissolution and recrystallization phenomena (Fig. S3(c) and (d)). The XRD patterns of the PVK-H.P. films at different dipping time were summarized in Fig. S3(b). When the drying pressure decreases to 1000 Pa, the decreased PS effectively decreases the intercalation reaction routing, which ultimately enhances the transformation process of PbI_2-M.P. film. Therefore, the PbI_2-M.P. film shows no residual PbI_2 after the dipping time of 60 s, and the XRD patterns of PVK-M.P. film at dipping time of 20 s and 40 s are summarized in Fig. S3(a). To clearly show the evolution of PbI_2 content in both PVK-H.P. film and PVK-M.P. film at different dipping time, the PbI_2 content is estimated according to Eq (S1), and the results are listed in Fig. 6. As can be seen in Fig. 6, both films show a rapid drop of residual PbI_2 content before dipping time of 60 s, and then, it shows a slow reaction process for the next almost 3 h for PVK-H.P. film, which may be attributed to transformation kinetics proceed from the surface to bottom of the perovskite film. When going on prolonging the dipping time of PbI_2-M.P. film, the dissolution and recrystallization of $CH_3NH_3PbI_3$ also occur (Fig. S4). In detail, when prolonging the dipping time to 3 min, the compact morphol-

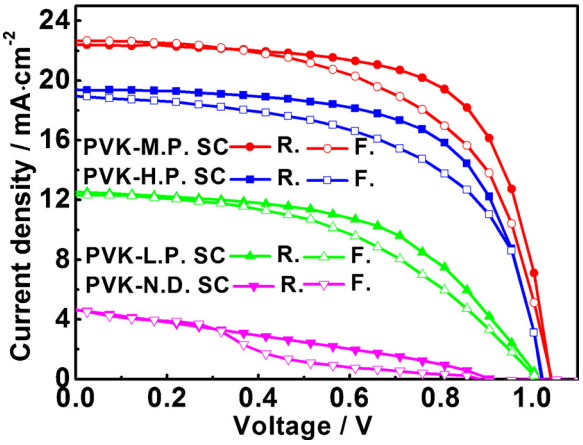

Fig. 7. *J-V* curves of the best PSCs assembled by PVK-N.D., PVK-H.P., PVK-M.P. and PVK-L.P under forward and reverse scan mode, where F. refers to forward scan mode, and R. refers to the reverse scan mode.

ogy of PVK-M.P. film is destroyed, and grain coarsening obviously occurs. When prolonging the dipping time to 5 min, some big perovskite grains begin to appear on film surface. When prolonging the dipping time to 10 min and 30 min, the big perovskite grains appearing on the film surface grow bigger and bigger. When the drying pressure goes on decreasing to 40 Pa, the PbI_2 film shows an increased PS even larger than PbI_2-H.P. and a contiguous morphology. One would expect that the transformation kinetics also proceed from the surface to bottom of the PbI_2 film as shown in Fig. 5. Therefore, there is a lot of residual PbI_2 in the final PVK-L.P. film.

3.4. Photovoltaic performance of planar configuration PSCs

To investigate the effect of perovskite films prepared by two-step solution method with PbI_2 film drying under various pressures, a series PSCs were fabricated. The optimal current density-voltage (*J-V*) curves of PSCs prepared with PbI_2 films under different drying conditions are shown in Fig. 7, and the detailed parameters for the solar cells are listed in Table S1. All the planar configuration PSCs have the device architecture of FTO/ZnO compact layer/perovskite film/Spiro-OMeTAD/Au as shown in Fig. S5. As it can be seen in Fig. 7, the PSC assembled by PVK-N.D. shows the lowest open-circuit voltage (V_{oc}) and lowest fill factor (FF), which could be attributed to the serious shunt recombination caused by the uncovered areas in the final perovskite films as shown in Fig. 1(a). The PSC assembled by PVK-L.P. shows a smaller short-circuit density (J_{sc}) compared with the PSCs assembled by PVK-H.P. and PVK-M.P. for its limited $CH_3NH_3PbI_3$ in the final perovskite film. All the photovoltaic parameters, including J_{sc}, V_{oc}, FF and power-conversion efficiency (PCE), of PVK-H.P. solar cell are smaller than PVK-M.P. solar cell. Considering the residual PbI_2 is reported to bring about a passivation effect as a built-in hole-blocking layer in perovskite solar cells, which may be advantageous for the photovoltaic conversion of the solar cell[39]. Therefore, to guarantee the average performance of both solar cells, more than twenty devices were prepared. As shown in Fig. 8, the statistical results of photovoltaic performance for all PVK-M.P. devices show an average J_{sc} of 19.28 ± 2.08 mA cm^{-2}, V_{oc} of 1.01 ± 0.03 V, FF of 0.61 ± 0.04 and thereby the PCE of 11.84 $\pm$1.51%. The result is higher than the performance of PVK-H.P. devices which show an average J_{sc} of 15.17 $\pm$5.51 mA cm^{-2}, V_{oc} of 0.87 $\pm$0.29 V, FF of 0.51 $\pm$0.13 and PCE of 7.63 $\pm$4.52%. Besides, the deviation of the photovoltaic parameters for PVK-M.P. solar cell is narrower than the PVK-H.P. solar cell. The lowest solar cell of PVK-M.P. shows a PCE of 9.87%, whereas

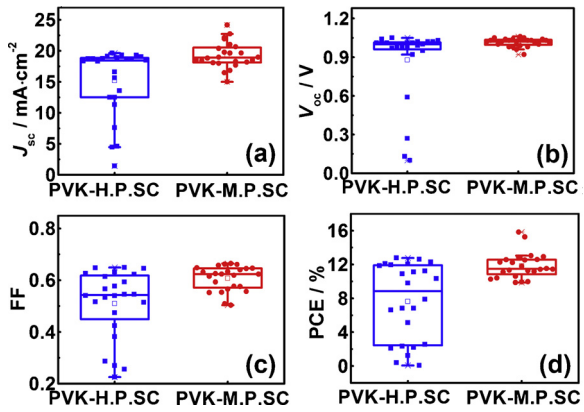

Fig. 8. Photovoltaic parameters distributions of PSCs assembled by PVK-H.P. and PVK-M.P.: (a) J_{sc}, (b) V_{oc}, (c) FF and (d) PCE.

0.4% for the PVK-H.P. solar cell. One typical EQE curves of PVK-H.P. solar cell and PVK-M.P. solar cell are also shown as Fig. S6. The PVK-M.P. solar cell shows higher EQE than the PVK-H.P. solar cell, which may attributed to the enhanced absorption ability of PVK-M.P. film (Fig. 4a) and/or the restrained charge recombination of PVK-M.P. solar cell.

The photovoltaic performance of both solar cells arising from the different perovskite films may be influenced by the charge transportation and recombination mechanism in the solar cells.

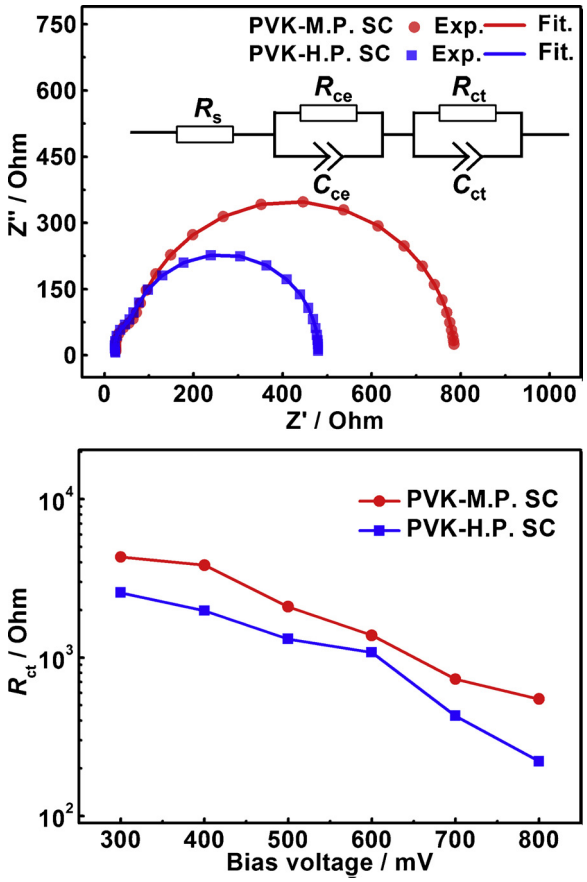

Fig. 9. Nyquist plots of PSCs assembled by PVK-H.P. and PVK-M.P. under a bias voltage of 400 mV (a), where scattered point: experimental data (Exp.), and solid line: fitting results (Fit.). The equivalent circuit is employed to fit the results (the inset of (a)). Plots of the recombination resistance (R_{ct}) vs. bias voltages for both PSCs (b).

Furthermore, the electrochemical impedance spectroscopy (EIS) was also carried out to investigate the charge transportation and recombination processes of both PSCs. Fig. 9(a) shows Nyquist plots for both solar cells, in which the potential bias is applied at 700 mV under illumination. Fig. 9(a) inset is the simplified transmission line model to fit the experimental results, in which R_{ce} and C_{ce} are supposed to the interface resistance and capacitance of the counter electrode, and R_{ct} and C_{ct} is the charge recombination resistance and capacitance of the perovskite film[40,41]. R_{ce} and R_{ct} are corresponding to the semi-arc in the Nyquist plot from left to right, separately. By fitting the Nyquist plots, the solar cell of PVK-M.P. possesses a larger R_{ct} of 731.1 ohm than the solar cell of PVK-H.P. (428.2 ohm), indicating restrained recombination of PVK-M.P. solar cell by using the PVK-M.P. film. In addition, the relationship between R_{ct} and the bias voltage is also obtained as Fig. 9(b), it can be seen that for both solar cells, R_{ct} decreases with the increasing forward bias voltage. At the same bias voltage, the R_{ct} of PVK-M.P. SC is larger than PVK-H.P. SC in all bias voltage ranges. The increased R_{ct} of PVK-M.P. SC compared with PVK-H.P. SC may be attributed to the improved film quality arising from high phase purity, high coverage ratio and good crystallization. In all, the micro-architecture of the PbI_2 film plays an important role for the final perovskite film quality, and we believe that a high quality perovskite film could be realized through a more suitable microstructure of the PbI_2 film by two-step solution method in future.

4. Conclusion

A series of PbI_2 films with tunable micro-architecture of PbI_2 crystals are prepared by solution processable crystal engineering. It was found the grain size of PbI_2 crystals and the corresponding pit spacing in the PbI_2 film decreased with decreasing the drying pressure to 1000 Pa. However, when going on decreasing the drying pressure to 40 Pa, the PbI_2 film showed uniform morphology with large pit spacing for the enhanced growth up after nucleation. After the dipping stage, the XRD patterns, UV–vis absorption and PL intensity illustrated that the perovskite film prepared by optimized pit spacing in gas pumped PbI_2 film at drying pressure of 1000 Pa showed the best film quality for its high phase purity, improved coverage ratio and good crystallization compared with the other perovskite films. A transformation kinetics showed that the pit spacing of the porous PbI_2 film strongly influenced the mass transfer and the sequential diffusion routing of CH_3NH_3I in the PbI_2 film, and the PbI_2 film could realize its full reaction state by decreasing the pit spacing in the film. At last, the PVK-M.P. solar cells showed improved PCEs and good reproducibility of photovoltaic performance for the restrained charge recombination arising from the high quality perovskite film. We think this architecture-tunable method of PbI_2 film and the transformation kinetics of PbI_2 into $CH_3NH_3PbI_3$ could contribute to the further study of the high performance PVK solar cells.

Acknowledgements

The authors acknowledge financial support from the National Program for Support of Top-notch Young Professionals.

References

[1] A. Kojima, K. Teshima, Y. Shirai, T. Miyasaka, J Am. Chem. Soc. 131 (2009) 6050–6051.
[2] H.S. Kim, C.R. Lee, J.H. Im, K.B. Lee, T. Moehl, A. Marchioro, S.J. Moon, R. Humphry-Baker, J.H. Yum, J.E. Moser, M. Gratzel, N.G. Park, Sci. Rep. 2 (2012) 591.
[3] M. Saliba, T. Matsui, K. Domanski, J.Y. Seo, A. Ummadisingu, S.M. Zakeeruddin, J.P. Correa-Baena, W.R. Tress, A. Abate, A. Hagfeldt, M. Gratzel, Science 354 (2016) 206–209.
[4] D.Q. Bi, C.Y. Yi, J.S. Luo, J.D. Decoppet, F. Zhang, S.M. Zakeeruddin, X. Li, A. Hagfeldt, M. Gratzel, Nat. Energy 1 (2016) 16142.
[5] S.-L. Chung, C.-M. Wang, J. Mater. Sci. Technol. 28 (2012) 713–722.
[6] K. Deng, L. Li, J. Mater. Sci. Technol. 32 (2016) 17–23.
[7] Y. Zhao, X. Li, Q. Li, C. Deng, J. Mater. Sci. Technol. 27 (2011) 764–768.
[8] W. Qiu, T. Merckx, M. Jaysankar, C.M. de la Huerta, L. Rakocevic, W. Zhang, U.W. Paetzold, R. Gehlhaar, L. Froyen, J. Poortmans, D. Cheyns, H.J. Snaith, P. Heremans, Energ. Environ. Sci. 9 (2016) 484–489.
[9] Y.C. Hsiao, T. Wu, M.X. Li, B. Hu, Adv. Mater. 27 (2015) 2899–2906.
[10] Q. Chen, N. De Marco, Y. Yang, T.B. Song, C.C. Chen, H.X. Zhao, Z.R. Hong, H.P. Zhou, Y. Yang, Nano Today 10 (2015) 355–396.
[11] H.J. Snaith, J. Phys Chem Lett, (2013) 3623–3630.
[12] B.E. Cohen, S. Gamliel, L. Etgar, APL Mater. 2 (2014) 081502.
[13] S. Yang, Y.C. Zheng, Y. Hou, X. Chen, Y. Chen, Y. Wang, H. Zhao, H.G. Yang, Chem. Mater. 26 (2014) 6705–6710.
[14] Y.P. Fu, F. Meng, M.B. Rowley, B.J. Thompson, M.J. Shearer, D.W. Ma, R.J. Hamers, J.C. Wright, S. Jin, J. Am. Chem. Soc. 137 (2015) 5810–5818.
[15] H. Zhang, J. Mao, H. He, D. Zhang, H.L. Zhu, F. Xie, K.S. Wong, M. Grätzel, W.C.H. Choy, Adv. Energ. Mater. 5 (2015) (n/a-n/a).
[16] F. Liu, Q. Dong, K.W. Man, A.B. Djurišić, A. Ng, Z. Ren, Q. Shen, C. Surya, W.K. Chan, J. Wang, Adv. Energ. Mater. 6 (2016).
[17] J. Burschka, N. Pellet, S.J. Moon, R. Humphry-Baker, P. Gao, M.K. Nazeeruddin, M. Gratzel, Nature 499 (2013) 316–320.
[18] Y. Wu, A. Islam, X. Yang, C. Qin, J. Liu, K. Zhang, W. Peng, L. Han, Energ. Environ. Sci. 7 (2014) 2934–2938.
[19] M.I. El-Henawey, R.S. Gebhardt, M.M. El-Tonsy, S. Chaudhary, J. Mater. Chem. A 4 (2016) 1947–1952.
[20] Q. Chen, H.P. Zhou, Z.R. Hong, S. Luo, H.S. Duan, H.H. Wang, Y.S. Liu, G. Li, Y. Yang, J. Am. Chem. Soc. 136 (2014) 622–625.
[21] Z.G. Xiao, Q.F. Dong, C. Bi, Y.C. Shao, Y.B. Yuan, J.S. Huang, Adv. Mater. 26 (2014) 6503–6509.
[22] J. Cao, F. Wang, H. Yu, Y. Zhou, H. Lu, N. Zhao, C.P. Wong, J. Mater. Chem. A 4 (2016) 10223–10230.
[23] J.J. Shi, Y.H. Luo, H.Y. Wei, J.H. Luo, J. Dong, S.T. Lv, J.Y. Xiao, Y.Z. Xu, L.F. Zhu, X. Xu, H.J. Wu, D.M. Li, Q.B. Meng, Acs Appl. Mater. Interf. 6 (2014) 9711–9718.
[24] F. Fu, L. Kranz, S. Yoon, J. Lockinger, T. Jager, J. Perrenoud, T. Feurer, C. Gretener, S. Buecheler, A.N. Tiwari, Phys. Status. Solidi a 212 (2015) 2708–2717.
[25] B. Ding, L. Gao, L. Liang, Q. Chu, X. Song, Y. Li, G. Yang, B. Fan, M. Wang, C. Li, Acs Appl. Mater. Interf. 8 (2016) 20067.
[26] Y. Li, X.L. He, B. Ding, L.L. Gao, G.J. Yang, C.X. Li, C.J. Li, J. Power Sources, (2016) 204–211.
[27] M. Mukhopadhyay, S.V. Dalvi, J. Chem. Technol. Biotechnol. 80 (2005) 445–454.
[28] S. Janarthanan, R.S. Samuel, S. Selvakumar, Y.C. Rajan, D. Jayaraman, S. Pandi, J. Mater. Sci. Technol. 27 (2011) 271–274.
[29] C.V. Thompson, Annu. Rev. Mater. Res. 16 (2000) 159–190.
[30] H. Lei, J. He, J. Mater. Sci. Technol. 28 (2012) 642–646.
[31] J.H. Im, I.H. Jang, N. Pellet, M. Grätzel, N.G. Park, Nat. Nanotechnol. 9 (2014) 927–932.
[32] D.Y. Liu, T.L. Kelly, Nat. Photon. 8 (2014) 133–138.
[33] I. Jeong-Hyeok, K. Hui-Seon, P. Nam-Gyu, APL Mater. 2 (2014) 081510.
[34] H.S. Ko, J.W. Lee, N.G. Park, J. Mater. Chem. A 3 (2015) 8808–8815.
[35] Y.Z. Xu, L.F. Zhu, J.J. Shi, X. Xu, J.Y. Xiao, J. Dong, H.J. Wu, Y.H. Luo, D.M. Li, Q.B. Meng, Chemphyschem 17 (2016) 112–118.
[36] Z.R. Zhang, X.P. Yue, D. Wei, M.C. Li, P.F. Fu, B.X. Xie, D.D. Song, Y.F. Li, RSC Adv. 5 (2015) 104606–104611.
[37] P.A. Beckmann, Cryst. Res. Technol. 45 (2010) 455–460.
[38] K.N. Liang, D.B. Mitzi, M.T. Prikas, Chem. Mater. 10 (1998) 403–411.
[39] Q. Chen, H.P. Zhou, T.B. Song, S. Luo, Z.R. Hong, H.S. Duan, L.T. Dou, Y.S. Liu, Y. Yang, Nano Lett. 14 (2014) 4158–4163.
[40] D.Y. Liu, J.L. Yang, T.L. Kelly, J. Am. Chem. Soc. 136 (2014) 17116–17122.
[41] J.X. Song, E.Q. Zheng, X.F. Wang, W.J. Tian, T. Miyasaka, Sol. Energ. Mater. Sol. C 144 (2016) 623–630.